

1 **Strong downdrafts preceding rapid tropopause ascent and their potential to**
2 **identify cross-tropopause stratospheric intrusions**

3 Feilong Chen¹, Gang Chen^{1*}, Chunhua Shi², Yufang Tian³, Shaodong Zhang¹,
4 Kaiming Huang¹

5 ¹School of Electronic Information, Wuhan University, Wuhan 430072, China.

6 ²Key Laboratory of Meteorological Disaster, Ministry of Education, Nanjing
7 University of Information Science & Technology, Nanjing 210044, China.

8 ³Key Laboratory of Middle Atmosphere and Global Environment Observation,
9 Institute of Atmospheric Physics, Chinese Academy of Sciences, Beijing 100029,
10 China

11 *Corresponding author: Gang Chen (g.chen@whu.edu.cn)

12
13 **Abstract:**

14 The capability of measuring 3-dimensional wind and tropopause structure with
15 relatively high time and vertical resolution makes VHF radar a potentially significant
16 tool for studying various processes of the atmosphere. **In the light of present**
17 **understanding, using VHF radars to identify possible stratospheric intrusions still**
18 **remain unclear.** Here the potential detection of stratospheric intrusion events is
19 discussed using the Beijing MST radar located at Xianghe (39.75°N, 116.96°E). During
20 the passage of a cut-off low in late November 2014, a deep V-shaped tropopause
21 structure, and strong downdrafts (>0.8 m/s) immediately preceding the rapid tropopause
22 ascent (>0.2 km/h) were observed. Within the height region of the downdrafts, **the**

23 **stability of the radar tropopause seems to be weakened.** Analysis results from global
24 reanalysis and the satellite data, as well as the trajectory model have shown the clear
25 evidence of the downward stratospheric intrusions (dry ozone-rich and depleted
26 methane air) associated with the strong downdrafts. Twenty typical cases of such strong
27 downdrafts, occurring during various synoptic processes in different seasons, have been
28 presented and **15 of them** are exactly associated with some form of stratospheric
29 intrusions. Four years (2012-2015) of such downdrafts are further discussed. The
30 observations reveal that the strong downdrafts preceding the rapid tropopause ascent
31 can be a valuable diagnostic for monitoring intrusion events, which will gain a better
32 understanding of stratospheric intrusions in VHF radar observations.

33

34 **Keywords:** Stratospheric intrusions; strong downdrafts; rapid tropopause ascent; MST
35 radar; VHF radar; cut-off low

36

37 1. Introduction

38 The tropopause is a stable transition zone separating the vertically stable stratified
39 stratosphere from the active free troposphere. The stratospheric and tropospheric air are
40 remarkably different in their chemical and dynamical characteristics. The stratosphere
41 is dominantly high in ozone and potential vorticity (PV) content and low in water vapor
42 (WV) and methane (CH₄) concentration, while the troposphere is just on the contrary
43 (Holton et al., 1995). Consequently, the natural stable tropopause layer, characterized
44 by strong gradients of trace constituents and wind speeds, plays an important role in
45 stratosphere-troposphere exchange (STE) processes. In other words, the layer is a
46 significant barrier for the atmospheric transport between stratosphere and troposphere
47 (Mahlman, 1997). From a long-term point of view, the seasonal variation of the
48 tropopause height determines the seasonal variation of the flux of stratospheric air into
49 the free troposphere (Appenzeller et al., 1996). Under the global climate warming (e.g.
50 the continuing rise in CO₂), the tropopause variation is also a significant factor that
51 must be considered with regards to the recovery of the stratospheric ozone (Butchart et
52 al., 2010; Chipperfield et al., 2017). On the other hand, the short-term tropopause
53 variability is sensitive to various meso- and small-scale atmospheric processes, during
54 which the folding/intrusion events commonly occur. This characteristic of the
55 tropopause change are sometimes directly used to detect the tropopause folds (e.g. Rao
56 et al., 2008; Alexander et al., 2012, and references therein), but are less, if any, directly
57 used to identify stratospheric intrusions. More detailed analysis of the variability of
58 high-resolution tropopause height and of course some other parameters (e.g. 3-

59 dimensional wind), and how the stratospheric **air is transported** across the tropopause
60 into the troposphere will help us to yield better understanding of the downward
61 stratospheric intrusions (e.g. Sprenger et al., 2003; Leclair de Bellevue et al., 2007; Das
62 et al., 2016).

63 **Although photochemical production within the troposphere is the main source of**
64 **tropospheric ozone**, the influence of the downward stratospheric intrusions on the
65 tropospheric ozone content cannot be ignored (Oltmans and Levy II, 1992; Stevenson
66 et al., 2006). Stratospheric intrusions bring dry ozone-rich air down into the free
67 troposphere (e.g. Stohl et al., 2000; Sørensen and Nielsen, 2001) and sometimes even
68 deep to the surface (e.g. Gerasopoulos et al., 2006; Grant et al., 2008; Jiang et al., 2015;
69 **Das et al., 2016**;). By now, it is well established that these intrusions of stratospheric
70 origin will significantly influence other trace gases (such as hydroxyl (OH)) in the
71 troposphere (Holton et al., 1995). These influences then will further contribute to the
72 change of radiative balance (Ramaswamy et al., 1992) and play an important role in the
73 radiative forcing of global climate change (Holton et al., 1995). It is true that
74 stratospheric intrusion events occur all over the world and in any season. However, they
75 are highly episodic in both vertical and isentropic (horizontal) directions (Chen, 1995).
76 Various dynamical and physical processes have been proposed to be responsible for
77 extra-tropical intrusion events. These mainly include tropopause folds, stratospheric
78 streamers and break-up, cut-off lows (COLs), wave breaking, and mesoscale convective
79 activities and thunderstorms (Stohl et al., 2003).

80 The certain dynamical and chemical characteristics of stratospheric air allow the

81 tracers, such as dry ozone-rich and high PV, to be proper indicators for the intrusions
82 penetrating down into the troposphere. Based on these tracers, various methods are
83 available to detect intrusion events. Balloon-borne ozonesonde sounding is an effective
84 tool to make measurements of ozone with high vertical resolution, but is limited by
85 coverage (He et al., 2011) and temporal resolution. In contrast, the satellite-borne
86 remote sensing instruments, such as Atmospheric Infrared Sounder (AIRS), can provide
87 nearly global coverage of various trace gases but have limitations in vertical and
88 temporal resolution. Another method for studying transport processes is trajectory
89 model, from which the backward trajectories can provide valuable information on the
90 possible sources of the trace gases (e.g. Elbern et al., 1997).

91 By far, large-scale STE has been widely studied and is fairly well understood, but
92 the details of small scale intrusions still need more researches (e.g. Holton et al., 1995).
93 Kumar and Uma (2009) reported that the shortage of direct measurements of vertical
94 winds near the tropopause may be responsible for the lack of fine-scale observations of
95 smaller scale intrusions.

96 Very-High-Frequency (VHF) radars, compared to the tools mentioned above, are
97 capable of continuously monitoring the atmosphere under any weather conditions and
98 detecting tropopause height from backscattered signal with both high temporal and
99 spatial resolution. During the past two decades, VHF radar measurements were
100 commonly used to assist to study the stratospheric intrusions (e.g. Hocking et al.,
101 2007; Das et al., 2016). However, it still remains uncertain in many aspects when
102 using only the VHF radar to identify intrusion events, especially the criteria for the

103 **identification.** Complicated and changeable atmospheric processes make it difficult
104 to identify the intrusion events by only radar data. The research by Hocking et al.,
105 (2007) have achieved a development in this issue. They found that the rapid ascent
106 in **RT altitude** (>0.2 km/h) can be a valuable diagnostic for possible stratospheric
107 intrusions **and the RT height started to ascent just when the stratospheric air intruded**
108 **across the tropopause layer.** However, it does not always work (e.g. He et al., 2011)
109 and remains uncertain when purely using the information of radar-determined
110 tropopause.

111 The central objective of the present study is to discuss the signature of downward
112 cross-tropopause intrusions using both the measurements of tropopause height and
113 vertical wind by the Beijing MST radar. This study is carried out mainly via a detailed
114 case observation during the passage of a COL and other general cases associated with
115 various atmospheric processes. Our discussion mainly focused on the potential of the
116 MST radar data to identify possible intrusion events, which is the main point of this
117 paper. In section 2 the datasets used in this paper are described, section 3 presents
118 detailed results and discussion, and section 4 gives the conclusions.

119

120 2. Dataset

121 2.1. MST radar data and tropopause detection

122 The Beijing MST radar located at Xianghe, China (39.75° N, 116.96° E, 22 m
123 above sea level) is a VHF radar operated at 50 MHz and installed in 2010 based on the
124 first phase of Chinese Meridian Space Weather Monitoring Project (Chinese Meridian
125 Project for short) (Wang, 2010). The radar antenna array consists of 24×24 three-
126 element Yagi to produce an average power aperture product of 3.2×10⁸ Wm² and
127 maximum directive gain of 34.8 dB. It operates radiation pattern with 172 kW peak
128 power and 3.2° half-power beam width. More detailed information of the radar system
129 can be found in Chen et al. (2016). Routine low mode data were used for present study
130 with 0.5 h time resolution and 1 μs coded pulse, which provides 150 m vertical
131 resolution. Details of the low mode setup used in this study are given in Table 1.

132 It has long been known that VHF radar reflectivity is proportional to the mean
133 generalized refractive index gradient M , which is a function of humidity variation and
134 static stability and given by (Ottersten, 1969) as follows

$$135 \quad M = -77.6 \times 10^{-6} (p/T) (d \ln \theta / dz) \\ 136 \quad \cdot \{ 1 + 15500 q / T [1 - (d \ln q / dz) / (2 d \ln \theta / dz)] \} \quad (1)$$

137 where p is the atmospheric pressure (hPa) T is the temperature (K), θ is the potential
138 temperature (K) and q is the specific humidity (gg⁻¹). According to the second and third
139 terms of the equation (1): large humidity variation contributes to the echo from the
140 lower and middle troposphere. From the first term: the radar backscatter power is
141 proportional to the static stability, which in fact is directly proportional to the potential

142 temperature gradient. The tropopause, near which a strong potential temperature
143 gradient exists, will lead to strong radar echoes in vertical incidence, as well as large
144 radar aspect sensitivity (as shown in Figure 1). Radiosonde data used in this paper were
145 received from the GTS1 type digital radiosonde launched from Beijing Meteorological
146 Observatory (39.93 °N, 116.28 °E, station number 54511), which is less than 45 km
147 away from the MST radar site. The black line in Fig.1 denotes the lapse-rate tropopause
148 (LRT) defined using the temperature lapse rate (World Meteorological Organization
149 (WMO), 1986). Applying the characteristic (enhanced radar echoes due to partial
150 specular reflection) mentioned above, the tropopause can be detected and its height
151 determined by VHF radars (Gage and Green, 1979). It has received widespread
152 application around the world, either in middle latitudes (e.g. Hocking et al., 2007), polar
153 regions (e.g. Alexander et al., 2012), and tropical regions (e.g. Yamamoto et al., 2003;
154 Das et al., 2008). Here, the radar-determined tropopause (RT) height is defined as the
155 height (above 500 hPa) where the maximum vertical gradient of echo power located
156 (shown as the orange circle in Figure 1a). This definition of RT is similar to that in the
157 studies of Alexander et al., [2012] and Ravindrababu et al., [2014].

158 In the present study, the MST radar mainly provides continuous measurements of
159 backscattered echo power, 3-D wind, and RT height with time resolution of 0.5 hour. In
160 addition, the radar aspect sensitivity, expressed as the ratio between vertical (p_v) and
161 oblique (p_o , here used the 15-degree north) beam echo power, is mainly caused by the
162 horizontally stratified anisotropic stable air and thus will be used as potential signature
163 of stratospheric intrusions in the troposphere (e.g. Kim et al., 2001). The backscattered

164 echo power given here is expressed as relative power in decibels (dB). In order to reduce
165 the random noise, the profile of p_v is smoothed by a 3-point running mean in altitude.
166 Note that the data that are heavily contaminated will be eliminated from our datasets.
167 The data of December 2015 and September 2015 are excluded.

168 2.2. AIRS satellite data

169 The AIRS instrument on NASA Aqua/EOS polar orbit satellite is a 2378 channel
170 nadir cross-track scanning infrared spectrometer. It can provide profiles of a number of
171 trace gases, including ozone and CH₄ (Susskind et al., 2003). The footprint of these
172 retrieval data is of 45 km by 45 km and their most sensitive region is in an altitude range
173 of 300-600 hPa. Many studies have shown that these AIRS retrieval constituents are
174 useful indicators for detecting stratospheric intrusions. He et al. [2011] suggested that
175 AIRS can observe the enhanced tropospheric ozone that is of stratospheric origin.
176 Xiong et al. [2013] reported that AIRS is capable of observing abnormal depletion in
177 CH₄ in the troposphere during intrusions. AIRS offers good latitude-longitude coverage.
178 Here we use version 6 of the AIRS Level-3 ozone and methane retrieval products.

179 2.3. Meteorological reanalysis

180 European Centre for Medium-Range Weather Forecasts (ECMWF) reanalysis
181 ERA-interim data are also used. After **November** 2000 the data are based on the
182 T511L60 version available with a 6-h temporal resolution and $3^\circ \times 3^\circ - 0.125^\circ \times$
183 0.125° latitude-longitude grid (Dee et al., 2011). The dataset from 15 isentropic and
184 37 pressure levels **interpolated into** $0.5^\circ \times 0.5^\circ$ grid are applied for present study.

185 2.4. HYSPLIT model

186 Backward (forward) trajectories in given starting locations are capable to
187 reproduce the sources (destinations) of the air parcel that will allow us to examine the
188 intrusions of stratospheric origin in the troposphere (e.g. Elbern et al., 1997). The
189 Hybrid Single Particle Lagrangian Integrated Trajectory model (HYSPLIT) developed
190 by the National Oceanic and Atmospheric Administration (NOAA)'s Air Resource
191 Laboratory (ARL) (Rolph, 2003; Stein et al., 2016) is applied to calculate the backward
192 and forward trajectories. The calculation method of the model is a hybrid between the
193 Lagrangian approach and the Eulerian methodology. In this paper, Global Data
194 Assimilation System (GDAS) datasets are adopted for driving the HYSPLIT.
195

196 **3. Results and discussion**

197 3.1. Meteorological synoptic situation

198 On the morning of 29 **November** 2014, a 500-hPa trough developed on the western
199 side of Lake Baikal (Western Siberia). The trough moved southeastward and extended
200 equatorward and its **southern tip** separated from the westerlies in the afternoon of 30
201 **November** 2014 (Fig. 2b), forming a COL near the radar site **as shown by the closed**
202 **geopotential contour**. The black stars in Figure 1 and other figures indicate the location
203 of the radar site. On the following days, the COL system moved northeastward
204 gradually (Fig. 2b) and finally stayed over eastern Russia near Sakhalin Island until it
205 reconnected and merged to the westerly flow. 315 K isentropic PV patterns have shown
206 the coarse resolution features of intrusions from the polar reservoir across the
207 tropopause into the midlatitude troposphere. The PV streamer curved and rolled up
208 cyclonically along the western flank of the COL (Fig.2b).

209 Fig. 3 shows the time series of hourly surface meteorological parameters over the
210 Beijing station. The data are obtained from the Chinese National Meteorology
211 Information Center and is less than 50 km from the MST radar site. As the dry-cold air
212 invasion accompanied with the COL travelled deeply into the planetary boundary layer,
213 it brought severe weather to the surface, including a rapid decrease in temperature and
214 humidity, and rapid increase in surface wind and sea level pressure. The humidity
215 decreased from ~85 to 12 percent within less than 8 hours. It is well established that the
216 polar-type COLs have strong potential to trigger deep convection (Price and Vaughan,
217 1993). To examine the potential convection, maps of high quality Climate Data Record

218 (CDR) of daily Outgoing Longwave Radiation (OLR) are displayed in Fig. 4. During
219 the development of the COL, a local region with abnormal low OLR value was clearly
220 observed near the radar site on 29 November (Fig. 4b). The Satellite-observed cloud
221 top temperature also showed the low values corresponding to the low OLR (figure not
222 shown), indicating that convection may be generated near radar side on 29 November.
223 Please note that we did not observe such low value either in OLR (Fig.4c, d) or in cloud
224 top temperature near the radar side on 30 November and 1 December. The time for all
225 the observations in this paper is shown in Universal Time (UTC) which is eight hours
226 behind Beijing standard time (LT=UTC+8).

227 3.2. MST radar observations

228 Radar echo power, horizontal wind vector, vertical wind, and radar aspect
229 sensitivity are plotted in Figure 5 as function of height and time during the passage of
230 the COL. Time variation of RT (black line) and LRT (black crosses) heights are also
231 displayed. The RT height first experienced a rapid descent, and then increased rapidly,
232 forming a deep V-shaped structure of ~4 km depth. The vertical velocity of the RT
233 height variation (both the rapid descent and ascent branches) reaches up to 0.28 km/h.
234 The rapid RT variation in altitude is in fact the response of the tropopause fold below
235 the jet stream, which will be well represented in Fig. 8a. Rapid variation in RT height
236 remained a region with low echo power (marked by R on Fig. 5a) and low aspect
237 sensitivity (marked by R' on Fig. 5d) where they should be normally high value within
238 the 'normal' tropopause layer. Unlike the RT height, the radiosonde LRT altitudes are
239 nearly constant during the COL passage. In normal conditions, RT agrees well with the

240 LRT altitude, such as indicated by Fig. 6a. However, large differences, of order of 2.5
241 km (as shown in Fig. 6b at 12 UTC 30 **November**), are observed between LRT and RT
242 in altitude during the passage of the COL as expected. It is the difference in definition
243 that contribute most to the large differences, especially under the tropopause fold
244 conditions (e.g. Yamamoto et al., 2003 and Fukao et al., 2003). It is worth noting that,
245 in Fig.6b, although there is no clear reversion in the radiosonde temperature profile
246 within the height of RT, the RT height exactly corresponds well to the reversion of
247 zonal and meridional wind and potential temperature gradient. Such differences
248 between RT and LRT heights can commonly be observed, especially during extreme
249 synoptic situations such as cyclone (e.g. Alexander et al., 2012).

250 The most important observation in this detailed case experiment is the strong
251 downdrafts (hereinafter inferred to as main downdrafts) observed immediately
252 preceding the rapid RT ascent (Fig.5c). The radar echo power sharply weakened (dotted
253 rectangle in Fig.5a) and the wind direction changed rapidly (Fig.5b, change from
254 dominant southerly wind to dominant northerly jet) within the height region of the main
255 downdrafts. As mentioned previously, abnormal low value in OLR and cloud top
256 temperature indicates the possible occurrence of convective activity on 29 **November**,
257 but nothing special appeared on 30 **November** near radar site. Consequently, we
258 preliminarily consider that the main downdrafts occurred near 07 UT 30 **November**
259 might not be produced directly by convective activity. Here, the accurate origin of the
260 main downdrafts will not be discussed in detail, and it is also beyond the scope of
261 present study.

262 The research by Hocking et al. (2007) has suggested that the rapid ascent in RT
263 height ($>0.2 \text{ km h}^{-1}$) can be a valuable predictor for the occurrence of stratospheric
264 intrusions. Here in this paper, the main downdrafts preceding the rapid RT ascent
265 observed by the Beijing MST radar are thus suspected to be an important feature or
266 response of some form of vertical stratospheric intrusions. Firstly, as the tropopause
267 descends (folded downward), it will displace stratospheric air into the troposphere (e.g.
268 Hoskins et al., 1985). Secondly, the main downdrafts will act as an effective way to
269 weaken the tropopause by means of continuously impinging on the tropopause, through
270 which the stratospheric air is permitted to penetrate down into the free troposphere (e.g.
271 Hirschberg and Fritsch, 1993; Kumar, 2006). In addition, after the main downdrafts,
272 the observed region near the upper troposphere with strong backscatter echoes (marked
273 by Q) and especially with abnormal high aspect sensitivity (marked by Q') may also be
274 a weak signature of the possible intrusions. In normal conditions, they are usually low
275 in value in the upper-troposphere (such as the region marked by P and P'). As we
276 mentioned before, the large value in radar aspect sensitivity is mainly caused by
277 reflection from stable atmospheric layer, such as the tropopause or lower-stratosphere.
278 When stable stratospheric air intrudes into the troposphere and without mixing with the
279 surrounding air mass, the intrusions in the free troposphere will be reflected as
280 abnormal large aspect sensitivity. Further direct evidence of the relevant intrusions in
281 dynamical and chemical aspects will be demonstrated in next section, using satellite
282 AIRS and global reanalysis data.

283 3.3. Associated stratospheric intrusions

284 Due to the sensitivity of the AIRS retrieved ozone and CH₄ is between 300-600
285 hPa. Fig. 7 shows the 500 hPa distribution of AIRS observed ozone and CH₄, along
286 with the AIRS tropopause contour (defined based on the temperature lapse-rate). The
287 ozone distribution maps (left panels of Fig. 7) clearly show a large area with enhanced
288 tropospheric ozone (>80 ppbv) near the radar site during the passage of the COL.
289 Moreover, severe CH₄ depletion (<1840 ppbv) was also observed (right panels in Fig.8).
290 These features of the ozone enhancement, CH₄ depletion, and the corresponding low
291 tropopause altitude clearly support the evidence of vertical downward cross-tropopause
292 stratospheric intrusions on 30 **November**.

293 The vertical cross-section of ECMWF PV and specific humidity at 1800 UT 30
294 **November** 2014 and the daily AIRS ozone on 30 **November** 2014, along a constant
295 latitude 40° N, is shown in Fig. 8. The corresponding vertical structure of the
296 stratospheric intrusions (dry ozone-rich and high PV along with low tropopause) over
297 regions near radar side is clearly seen. The specific humidity tracer displays less distinct
298 structure as compared with the other two tracers (similar as that shown by Vérémes et
299 al., 2016). The cross-section of PV in Fig. 8a have demonstrated relatively finer-scale
300 structure of the stratospheric PV intrusions (below the jet stream), which penetrated
301 down deeply into ~650 hPa (~3.6 km).

302

303 3.4. Trajectory model analysis

304 Figure 9 shows 30h backward trajectories ending at the radar site at 18 UT 29
305 **November** (left panel) and at 18 UT 30 **November** (right panel). As expected, the air

306 masses parcel transported eastward horizontally before the occurrence of main
307 downdrafts (fig.10a). Whereas after the downdrafts, the trajectories clearly show that
308 the tropospheric air masses over the radar site are of stratospheric origin from the
309 western side of Lake Baikal. Trajectory results further support the evidence of
310 stratospheric intrusions that closely related with the main downdrafts.

311 On the other hand, 30-h forward trajectories starting at 00 UT 30 November (left
312 panel) and 00 UT 1 December (right panel) are shown in Fig. 10. It is interesting to note
313 that, from Fig.11a before the passage of COL, the air parcels at 4 km transport rapidly
314 upward (by more than 4 km within ~23 h) and northeastward to the upper-troposphere
315 of East Siberian. This upward and poleward transportation is associated with a warm
316 conveyor belt (southerly flows dominate) that is located ahead of the COL. It
317 contributes to transporting the tropospheric moist and polluted air (such as aerosol) into
318 the upper-troposphere and even the lower stratosphere (e.g. Stohl et al., 2003; Sandhya
319 et al., 2015). After the downdrafts, forward trajectories in fig.11b demonstrate that the
320 dry intrusion air parcels continue to be transported downward and southeastward to the
321 boundary layer or even the surface.

322 3.5. Strong downdrafts preceding rapid tropopause ascent and discussion

323 Figure 11a shows another 20 typical cases of strong downdrafts preceding rapid
324 RT ascent for the period March 2012 and Jan. 2015 (shown placed end-to-end), the
325 LRT height (plotted in crosses) and the vertical velocity of the RT (plotted in orange
326 line) is also plotted. These cases (marked by black rectangular boxes and labeled as S1,
327 S2, S3..., and S20) are identified based on the following criteria: 1) the amplitude of

328 the RT ascent should exceed 0.6 km (four range gates), 2) vertical velocities of the RT
329 ascent excess 0.1 km/h, 3) the downdrafts occurred preceding the RT ascent **should >0.5**
330 m/s, and the height region of the downdrafts should pass through the RT layer. The
331 criteria are put forward mainly to avoid the influence of the RT spikes. Figure 11b
332 **shows the backward trajectories for the selected 9 cases.** Results show clear evidence
333 of **downward intrusions** corresponding to the associated strong downdrafts. Their
334 sources are mainly from West Siberia (western side of Lake Baikal), except for the case
335 Tr5. Moreover, according to AIRS daily 500 hPa ozone distribution, **most of the cases**
336 in Figure 11a (except for the cases S14, S15, S16, S17, S20) were **associated with**
337 **significant ozone enhancement**, indicating intrusions of stratospheric origin (as shown
338 in **Supplementary figure S1**). It is important to note that the RT excursion velocity of
339 all the cases is not all above 0.2 km/h and some are lower than this value (**e.g. cases**
340 **S16 and S18**). However, some form of stratospheric intrusions **was** exactly observed in
341 **such cases** from both the trajectory and satellite results. Therefore, the threshold of
342 vertical velocity of the RT **ascent** is set at 0.1 km/h, rather than 0.2 km/h (Hocking et
343 al., 2007). Large differences between RT and LRT are also interesting to be noted on
344 some occasions when the RT changes rapidly (such as the occasion near 14 March
345 2012).

346 According to the meteorological chart, the synoptic situation of those cases
347 identified in **Fig. 11a** are introduced. The **cases S1, S2, S8, S9, S10, and S11** seem to
348 have a close relationship with COL development; **cases S3, S4, S5, S6, S7, S17, S18,**
349 **and S19** seem associated with low or high **trough systems (at 500 hPa)**. The remaining

350 cases seem not associated with any significant synoptic development. However, in
351 terms of the distribution of isentropic PV (generally at 315K in winter and 330K in
352 summer), we found that the remaining cases S12, S13, S14, S15, S16, and S20 appear
353 to be associated with some form of stratospheric streamers and their break-up within
354 the previous 48h (not shown). Some cases (e.g. S1 and S2) that appear close on the
355 same day were probably caused by the same system. The characteristics of the 20 cases,
356 including background synoptic condition, vertical velocity of the RT ascent, and 500
357 hPa ozone enhancement, have been summarized in Table 2.

358 In the light of present understanding, the strong downdrafts preceding the rapid
359 RT ascent can serve as an important diagnostic for intrusion events, during various
360 synoptic processes in any season. This characteristic will be of great use and play an
361 important role in routine identification of stratospheric intrusions. Considering the
362 duration of such downdrafts, a higher time resolution of radar observations will be more
363 helpful. Present study has shown the duration of the majority downdrafts is generally
364 within 1.5-3 hours. We consider, therefore, that the radar resolution should be best
365 within 1h.

366 Although Hocking et al. (2007) have reported that the rapid tropopause ascent
367 (>0.2 km/h) alone can be a useful diagnostic for potential intrusion events. However,
368 using only the information of RT heights might lead to non-negligible errors, as
369 mentioned above in introduction and according to the observations in Fig. 11.
370 Especially on occasions when the RT ascent is between 0.1-0.2 km/h but the
371 corresponding true intrusions were observed, all such intrusion events will be neglected

372 (maybe ~ 2 per month, refer to Fig. 12a). Whereas on some occasions when the RT
373 ascent **exceeds** 0.2 km/h, but without observing true intrusion events (e.g. He et al.,
374 2011), these events will be misdiagnosed (maybe ~ 13 per month, refer to Fig. 12b). In
375 this sense, using the unique MST radar observations of both the RT height variability
376 and the vertical wind as complementary signature for identifying possible intrusion
377 events is very meaningful.

378 Figure 12 shows four years (2012-2015) of the events with rapid RT ascent (gray
379 bands), and the events with strong downdrafts just preceding the rapid RT ascent (black
380 bands). The identification criteria of such strong downdrafts are similar to that
381 mentioned above and the events are classified according to different value of vertical
382 velocity of the ascent. Among all the events with ascent velocity between 0.1-0.2 km/
383 h, about one-quarter (approximate 2 per month, Fig. 12a) were observed with strong
384 downdrafts preceding them. Whereas, as for the events with the ascent velocity >0.2
385 km/h, the proportion is about a half (approximate 10 per month, Fig. 12b). Here,
386 according to the results above, the occurrence of the strong downdrafts just preceding
387 the rapid RT ascent (black bands in Fig. 12) to a large degree represents the occurrence
388 of possible intrusions. In this way, Fig. 12 indicates that the occurrence of possible
389 intrusions exhibit distinct seasonal variations, with a maximum in winter and spring
390 minimum in summer. This is because the meso- and small-scale atmospheric processes,
391 such as cold air outbreaks, thunderstorms, and convective activities, are more active in
392 winter and spring. They are important sources for downward stratospheric intrusions.

393

394 4. Conclusions

395 Detailed case analysis of the cross-tropopause stratospheric intrusions was carried
396 out during a COL. Global reanalysis, satellite data, and HYSPLIT trajectories all
397 showed consistent evidences of dry ozone-rich, high PV, and depleted CH₄ air that have
398 penetrated downward into the free troposphere. The key signature of the stratospheric
399 intrusions in the Beijing MST radar observations is the strong downdrafts just preceding
400 rapid RT ascent. The radar echo power decreased rapidly within the region of strong
401 downdrafts, after which abnormal high aspect sensitivity was recorded in troposphere.
402 Such high aspect sensitivity is served as another potential clue for the intrusions of
403 stratospheric origin.

404 Based on the criteria mentioned in section 3.5, other 20 typical cases of strong
405 downdrafts preceding the rapid RT ascent between March 2012 and Jan. 2015 were
406 presented. These events occurred during different synoptic processes in different
407 seasons. **Yet, most of the cases (15 of them)** are associated with some form of intrusions
408 observed by combination of **AIRS-retrieved** ozone and the HYSPLIT trajectory model.
409 Our results show that the **radar-derived** tropopause height and vertical winds are strong
410 complementary indicators to be used to infer the occurrence of the intrusions of
411 stratospheric origin. This will be of great use and play an important role for the routine
412 identification or prediction of intrusion events. However, the actual origin of the
413 observed downdrafts preceding the rapid RT ascent is not addressed in this paper.
414 Further combination observational experiments need to be conducted, especially
415 combined using ozonesonde soundings, to quantitative analyze the effectiveness of

416 present identification criteria for possible intrusions.

417

418

419 **Acknowledgment**

420 The authors really appreciate Prof Shira Raveh-Rubin for reading and checking the
421 manuscript, using the criterion in Raveh-Rubin, 2017. This work is funded by National
422 Natural Science Foundation of China (NSFC grants No. 41722404 and 41474132). The
423 authors would like to thanks the technical and scientific staff of Chinese Meridian Space
424 Weather Monitoring Project (CMSWMP) for their support in conducting the
425 experiment. The authors sincerely acknowledge the ECMWF, NASA, and NOAA Air
426 Resources Laboratory (ARL) for providing global reanalysis, satellite trace gases, and
427 HYSPLIT transport model, respectively. The MST radar data for this paper are
428 available at Data Centre for Meridian Space Weather Monitoring Project
429 (<http://159.226.22.74/>). The radiosonde data is available from
430 <http://weather.uwyo.edu/upperair/sounding.html>.

431

432 **References**

- 433 Appenzeller, C., Holton, J. R., & Rosenlof, K. H.: Seasonal variation of mass transport
434 across the tropopause. *Journal of Geophysical Research Atmospheres*, 101(D10),
435 15071–15078, 1996.
- 436 Appenzeller, C., Davies, H. C., & Norton, W. A.: Fragmentation of stratospheric
437 intrusions. *Journal of Geophysical Research Atmospheres*. 101(D1), 1435-1456,
438 1996.
- 439 Alexander, S. P., Murphy, D. J., and Klekociuk, A. R.: High resolution VHF radar
440 measurements of tropopause structure and variability at Davis, Antarctica (69° S,
441 78° E). *Atmospheric Chemistry and Physics*, 13(12), 26173-26205, 2012.
- 442 Bonasoni, P., Evangelisti, F., Bonafe, U., Ravegnani, F., Calzolari, F., Stohl, A., Tositti
443 L., Tubertini O., & Colombo, T.: Stratospheric ozone intrusion episodes recorded
444 at Mt. Cimone during the VOTALP project: case studies. *Atmospheric*
445 *Environment*, 34(9), 1355-1365, 2000.
- 446 Butchart, N., Cionni, I., Eyring, V., Shepherd, T. G., Waugh, D. W., & Akiyoshi, H.,
447 et al.: Chemistry-climate model simulations of twenty-first century stratospheric
448 climate and circulation changes. *Journal of Climate*, 23(20), 5349-5374, 2010.
- 449 Chipperfield, M. P., Bekki, S., Dhomse, S., Harris, N., Hassler, B., & Hossaini, R., et
450 al.: Detecting recovery of the stratospheric ozone layer. *Nature*, 549(7671), 211-
451 218, 2017.
- 452 Chen, P.: Isentropic cross-tropopause mass exchange in the extratropics. *Journal of*
453 *Geophysical Research*, 16661-16673, 1995.

454 Chen, G., Cui, X., Chen, F., Zhao, Z., Wang, Y., Yao, Q., ... & Gong, W.: MST Radars
455 of Chinese Meridian Project: System Description and Atmospheric Wind
456 Measurement. *IEEE Transactions on Geoscience and Remote Sensing*, 54(8),
457 4513-4523, 2016.

458 Das, S. S., A. R. Jain, K. K. Kumar, and D. Narayana Rao: Diurnal variability of the
459 tropical tropopause: Significance of VHF radar measurements, *Radio Sci.*, 43,
460 RS6003, doi:10.1029/2008RS003824, 2008.

461 Das, S. S., Ratnam, M. V., Uma, K. N., Patra, A. K., Subrahmanyam, K. V., Girach, I.
462 A., Suneeth K. V. , Kumar K. K., & Ramkumar, G.: Stratospheric intrusion into
463 the troposphere during the tropical cyclone Nilam (2012). *Quarterly Journal of the*
464 *Royal Meteorological Society*, 142(698), 2168-2179, 2012.

465 Das, S.S., M. V. Ratnam, K. N. Uma, K. V. Subrahmanyam, I.A.Girach, A. K. Patra,S.
466 Aneesh, K.V. Suneeth, K. K. Kumar, A.P.Kesarkar, S. Sijikumar and G.
467 RamkuMarch.: Influence of Tropical Cyclones on Tropospheric Ozone: Possible
468 Implications (2016), *Atmospheric Chemistry and Physics*, 16, 4837-4847, 2016.

469 Dee, D. P., Uppala, S. M., Simmons, A. J., Berrisford, P., Poli, P., & Kobayashi, S., et
470 al.: The era - interim reanalysis: configuration and performance of the data
471 assimilation system. *Quarterly Journal of the Royal Meteorological Society*,
472 137(656), 553-597, 2011.

473 Elbern, H., Kowol, J., Sládkovic, R., & Ebel, A.: Deep stratospheric intrusions: a
474 statistical assessment with model guided analyses. *Atmospheric Environment*,
475 31(19), 3207-3226, 2006.

476 Fukao, S., H. Hashiguchi, M. Yamamoto, T. Tsuda, T. Nakamura, M. K. Yamamoto,
477 T. Sato, M. Hagio, and Y. Yabugaki.: Equatorial Atmosphere Radar (EAR).:
478 System description and first results, *Radio Sci.*, 38(3), 1053,
479 doi:10.1029/2002RS002767, 2003.

480 Gage, K. S., & Green, J. L.: Tropopause detection by partial specular reflection with
481 Very-High-Frequency radar. *Science*, 203(4386), 1238-40, 1979.

482 Gerasopoulos, E., Zanis, P., Papastefanou, C., Zerefos, C.S., Ioannidou, A., Wernli, H.:
483 A complex case study of down to the surface intrusions of persistent stratospheric
484 air over the Eastern Mediterranean. *Atmospheric Environment*, 40(22), 4113-4125,
485 2006.

486 Grant, Deanne, Jose D. Fuentes, Marcia S. DeLonge, Stephen Chan, Everette Joseph,
487 Paul Kucera, Seydi A. Ndiaye, Amadou T. Gaye (2008), Ozone transport by
488 mesoscale convective storms in western Senegal, *Atmos. Envir.*, 42, 7104–7114,
489 doi:10.1016/j.atmosenv.2008.05.044

490 He, H., Tarasick, D. W., Hocking, W. K., Careysmith, T. K., Rochon, Y. J., Zhang, J., ...
491 & Bourqui, M. S.: Transport analysis of ozone enhancement in Southern Ontario
492 during BAQS-Met. *Atmospheric Chemistry and Physics*, 11(6), 2569-2583, 2011.

493 Hocking, W. K., Careysmith, T., Tarasick, D. W., Argall, P. S., Strong, K., Rochon, Y.
494 J., Zawadzki Irek & Taylor, P. A.: Detection of stratospheric ozone intrusions by
495 windprofiler radars. *Nature*, 450(7167), 281-284, 2007.

496 Holton, J. R., P. H. Haynes, M. E. McIntyre, A. R. Douglass, R. B. Rood, and L. Pfister:
497 Stratosphere-troposphere exchange, *Reviews of Geophysics*, 33(4), 403–439,

498 doi:10.1029/95RG02097, 1995.

499 Hoskins B.J., McIntyre M.E., Robertson A.W.: On the use and significance of
500 isentropic potential vorticity maps. *Q. J. R. Meteorol. Soc.* 111: 877–946. 1985.

501 Hirschberg, P. A., and J. M. Fritsch: A study of the development of extratropical
502 cyclones with an analytic model. Part I: The effects of stratospheric structure,
503 *Journal of the Atmospheric Sciences*, 50, 311 –327, doi:10.1175/1520-
504 0469(1993)050<0311:ASOTDO>2.0.CO;2, 1993.

505 Jiang, Y. C., T. L. Zhao, J. Liu, X. D. Xu, C. H. Tan, X. H. Cheng, X. Y. Bi⁶, J. B. Gan,
506 J. F. You, and S. Z. Zhao (2015), Why does surface ozone peak before a typhoon
507 landing in southeast China? *Atmos. Chem. Phys.*, 15, 13331–13338,
508 doi:10.5194/acp-15- 13331-2015

509 Kim, K. E., Jung, E. S., Campistron, B., & Heo, B. H.: A physical examination of
510 tropopause height and stratospheric air intrusion: a case study. *Journal of the*
511 *Meteorological Society of Japan*, 79(5), 1093-1103, 2001.

512 Kumar, K. K., & Uma, K. N.: High temporal resolution VHF radar observations of
513 stratospheric air intrusions in to the upper troposphere during the passage of a
514 mesoscale convective system over gadanki (13.5° n, 79.2° e). *Atmospheric*
515 *Chemistry & Physics*, 24(8), 14-17, 2009.

516 Kumar, K. K.: VHF radar observations of convectively generated gravity waves: Some
517 new insights. *Geophysical Research Letters*, 33(1), doi:10.1029/2005GL024109,
518 2006.

519 Leclair de Bellevue J, Baray JL, Baldy S, Ancellet G, Diab R, Ravetta F.: Simulations

520 of stratospheric to tropospheric transport during the tropical cyclone Marlene
521 event. *Atmospheric Environment*, **41**: 6510–6526, doi:
522 10.1016/j.atmosenv.2007.04.040, 2007.

523

524 Mahlman, J. D.: Dynamics of transport processes in the upper troposphere. *Science*,
525 276(5315), 1079-1083, 1997.

526 Mihalikova, M., Kirkwood, S., Arnault, J., & Mikhaylova, D.: Observation of a
527 tropopause fold by MARA VHF wind-profiler radar and ozonesonde at Wasa,
528 Antarctica: comparison with ECMWF analysis and a WRF model simulation.
529 *Annales Geophysicae*, 30(9), 1411-1421, 2012.

530 Nastrom, G. D., Green, J. L., Gage, K. S., & Peterson, M. R.: Tropopause folding and
531 the variability of the tropopause height as seen by the flatland VHF radar. *Journal*
532 *of Applied Meteorology*, 28(12), 1271-1281, 1989.

533 Oltmans, S. J., and H. Levy II.: Seasonal cycle of surface ozone over the western North
534 Atlantic, *Nature*, 358, 392–394, 1992.

535 Ottersten, H.: Mean vertical gradient of potential refractive index in turbulent mixing
536 and radar detection of CAT, *Radio Science*, 4, 1247–1249,
537 doi:10.1029/RS004i012p01247, 1969.

538 Price, J. D., & Vaughan, G.: The potential for stratosphere-troposphere exchange in cut-
539 off-low systems. *Quarterly Journal of the Royal Meteorological Society*, 119(510),
540 343-365, 1993.

541 Rao, T. N., and S. Kirkwood: Characteristics of tropopause folds over Arctic latitudes,

542 Journal of Geophysical Research, 110, D18102, doi:10.1029/2004JD005374,
543 2005.

544 Rao, T. N., Arvelius, J., & Kirkwood, S.: Climatology of tropopause folds over a
545 european arctic station (esrange). Journal of Geophysical Research Atmospheres,
546 113(D7), 762-770, 2008.

547 Ravindrababu, S., Venkat Ratnam, M., Sunilkumar, S. V., Parameswaran, K., and
548 Krishna Murthy, B. V.: Detection of tropopause altitude using Indian MST radar
549 data and comparison with simultaneous radiosonde observations. Journal of
550 Atmospheric and Solar-Terrestrial Physics, 121(6), 679-687, 2014.

551 Ramaswamy V, Schwarzkopf MD, Shine KP.: Radiative forcing of climate from
552 halocarbon-induced global stratospheric ozone loss. Nature **355**: 810–812, doi:
553 10.1038/355810a0, 1992.

554 Rolph, G.D.: Real-time Environmental Applications and Display sYstem (READY)
555 Website. NOAA Air Resources Laboratory, Silver Spring, MD. [http://](http://www.arl.noaa.gov/ready/hysplit4.html)
556 www.arl.noaa.gov/ready/hysplit4.html, 2003.

557 Sandhya, M., Sridharan, S., & Indira Devi, M.: Tropical upper tropospheric humidity
558 variations due to potential vorticity intrusions. Annales Geophysicae, 33(9), 1081-
559 1089, 2015.

560 Skerlak, B., Sprenger, M., Pfahl, S., Tyrlis, E., & Wernli, H.: Tropopause folds in ERA-
561 Interim: Global climatology and relation to extreme weather events. Journal of
562 Geophysical Research, 120(10), 4860-4877, 2015.

563 Stohl, A., Bonasoni, P., Cristofanelli, P., Collins, W., Feichter, J., & Frank, A., et al.:

564 Stratosphere-troposphere exchange: a review, and what we have learned from
565 staccato. *Journal of Geophysical Research Atmospheres*, 108(D12), 469-474,
566 2003.

567 Stohl, A., et al.: The influence of stratospheric intrusions on alpine ozone concentrations,
568 *Atmospheric Environment*, 34, 1323– 1354, 2000.

569 Stohl, A., Wernli, H., James, P., Bourqui, M., Forster, C., & Liniger, M. A., et al.: A new
570 perspective of stratosphere troposphere exchange. *Bulletin of the American*
571 *Meteorological Society*, 84(11), 2003.

572 Stein, A. F., Draxler, R. R., Rolph, G. D., Stunder, B. J. B., Cohen, M. D., & Ngan, F.:
573 NOAA's HYSPLIT atmospheric transport and dispersion modeling system. *Bulletin*
574 *of the American Meteorological Society*, 96(12), 150504130527006, 2016.

575 Stevenson, D. S., Dentener, F. J., Schultz, M. G., Ellingsen, K., Noije, T. P. C. V., &
576 Wild, O., et al.: Multimodel ensemble simulations of present-day and near-future
577 tropospheric ozone. *Journal of Geophysical Research Atmospheres*, 111(D8), 263-
578 269, 2006.

579 Sørensen, J. H., and Nielsen, N. W.: Intrusion of stratospheric ozone to the free
580 troposphere through tropopause folds -a case study. *Physics and Chemistry of the*
581 *Earth Part B Hydrology Oceans and Atmosphere*, 26(10), 801-806, 2001.

582 Su, L., Yuan, Z., Fung, J. C., & Lau, A. K.: A comparison of HYSPLIT backward
583 trajectories generated from two GDAS datasets. *Science of The Total Environment*,
584 527-537, 2015.

585 Susskind, J., C. D. Barnett, and J. M. Blaisdell.: Retrieval of atmospheric and surface

586 parameters from AIRS/AMSU/HSB data in the presence of clouds, IEEE
587 Transactions on Geoscience and Remote Sensing, 41(2), 390–409,
588 doi:10.1109/tgrs.2002.808236, 2003.

589 Vaughan, G., Gouget, H., O'Connor, F. M., & Wier, D.: Fine-scale layering on the edge
590 of a stratospheric intrusion. Atmospheric Environment, 35(12), 2215–2221, 2001.

591 Vèrèmes, H., J.-P. Cammas, J.-L. Baray, P. Keckhut, C. Barthe, F. Posny, P. Tulet, D.
592 Dionisi, and S. Bielli: Multiple subtropical stratospheric intrusions over Reunion
593 Island: Observational, Lagrangian, and Eulerian numerical modeling approaches,
594 Journal of Geophysical Research Atmospheres, 121, 14,414–14,432, doi:10.1002/
595 2016JD025330, 2016.

596 Wang, C.: New Chains of Space Weather Monitoring Stations in China. Space Weather-
597 the International Journal of Research and Applications, 8(8), 2010.

598 World Meteorological Organization (WMO): Atmospheric ozone 1985, WMO Global
599 Ozone Res. and Monit. Proj. Rep. 20, Geneva, Switzerland, 1986.

600 Xiong, X., C. Barnet, E. Maddy, S. C. Wofsy, L. Chen, A. Karion, and C. Sweeney.:
601 Detection of methane depletion associated with stratospheric intrusion by
602 atmospheric infrared sounder (AIRS), Geophysical Research Letters, 40, 2455–
603 2459, doi:10.1002/grl.50476, 2013.

604 Yamamoto, M., Oyamatsu, M., Horinouchi, T., Hashiguchi, H., & Fukao, S.: High time
605 resolution determination of the tropical tropopause by the Equatorial Atmosphere
606 Radar. Geophysical Research Letters, 30(21), 2003.

607

608 **Table**

Radar parameter	Value
Transmitted frequency	50 MHz
Antenna array	24×24 3-element Yagi
Antenna gain	33 dB
Transmitter peak power	172.8 kW
Code	16-bit complementary
No. coherent integrations	128
No. FFT points	256
No. spectral average	10
Pulse repetition period	160 μs
Half power beam width	3.2°
Pulse length	1 μs
Range resolution	150 m
Temporal resolution	30 min
Off-zenith angle	15°

609 **Table 1.** Operating parameters in low-mode of the Beijing MST radar.

610

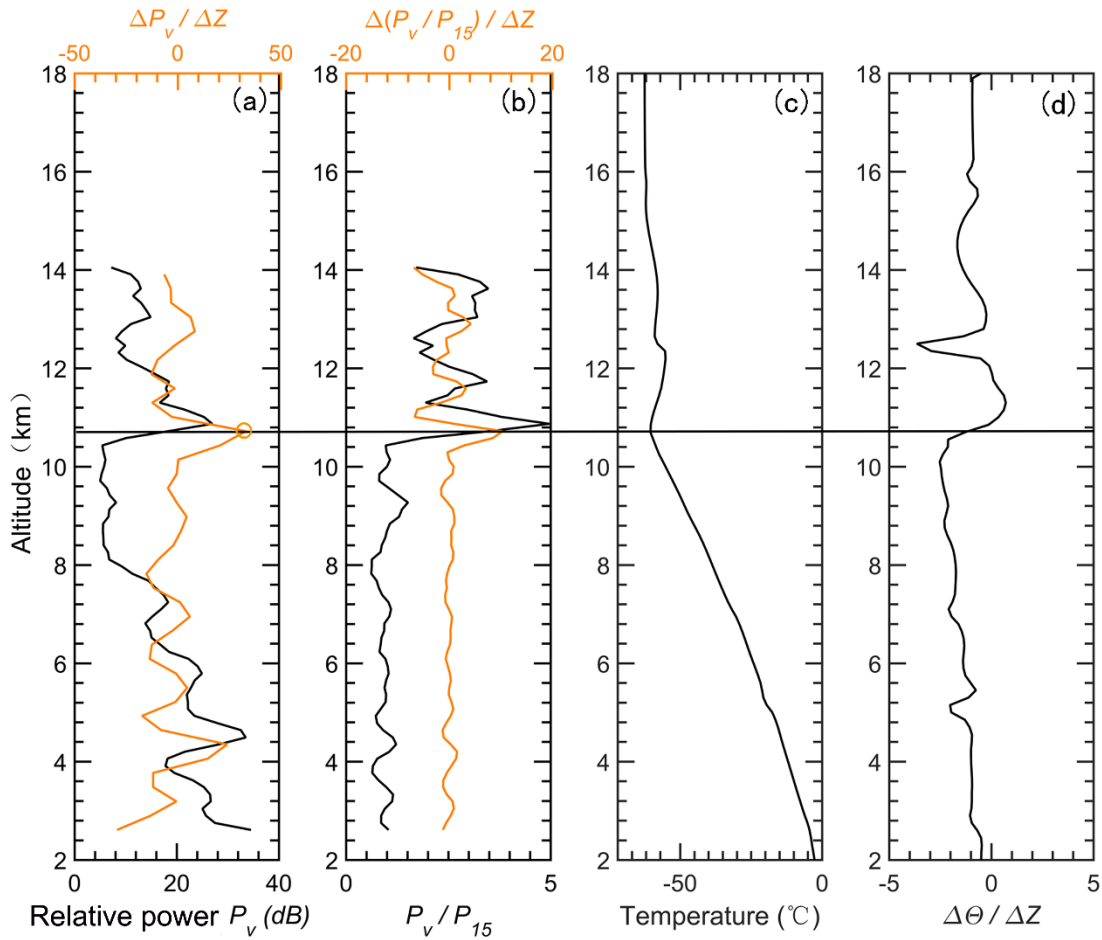
Cases	Time (year/month/day)	Background condition	Vertical velocity of RT ascent	500 hPa ozone enhancement
S1	2012/03/06	Cut-off low	>0.2 km/h	Enhanced
S2	2012/03/06	Cut-off low	>0.2 km/h	Enhanced
S3	2012/03/12	Low/high trough	>0.2 km/h	Enhanced
S4	2012/03/13	Low/high trough	>0.2 km/h	Enhanced
S5	2012/04/05	Low/high trough	>0.2 km/h	Enhanced
S6	2012/04/05	Low/high trough	>0.2 km/h	Enhanced
S7	2012/04/06	Low/high trough	>0.2 km/h	Enhanced
S8	2012/06/13	Cut-off low	>0.2 km/h	Enhanced
S9	2012/06/13	Cut-off low	>0.2 km/h	Enhanced
S10	2013/08/02	Cut-off low	>0.2 km/h	Enhanced
S11	2013/08/02	Cut-off low	>0.2 km/h	Enhanced

S12	2013/08/03	PV streamer	>0.2 km/h	Enhanced
S13	2013/08/03	PV streamer	>0.2 km/h	Enhanced
S14	2014/01/02	PV streamer	>0.2 km/h	None
S15	2014/01/02	PV streamer	>0.2 km/h	None
S16	2014/01/03	PV streamer	0.1-0.2 km/h	None
S17	2014/01/04	Low/high trough	>0.2 km/h	None
S18	2014/05/02	Low/high trough	0.1-0.2 km/h	Enhanced
S19	2014/05/02	Low/high trough	>0.2 km/h	Enhanced
S20	2015/01/03	PV streamer	>0.2 km/h	None

611 **Table 2.** Characteristics of the 20 cases shown in Fig. 11a.

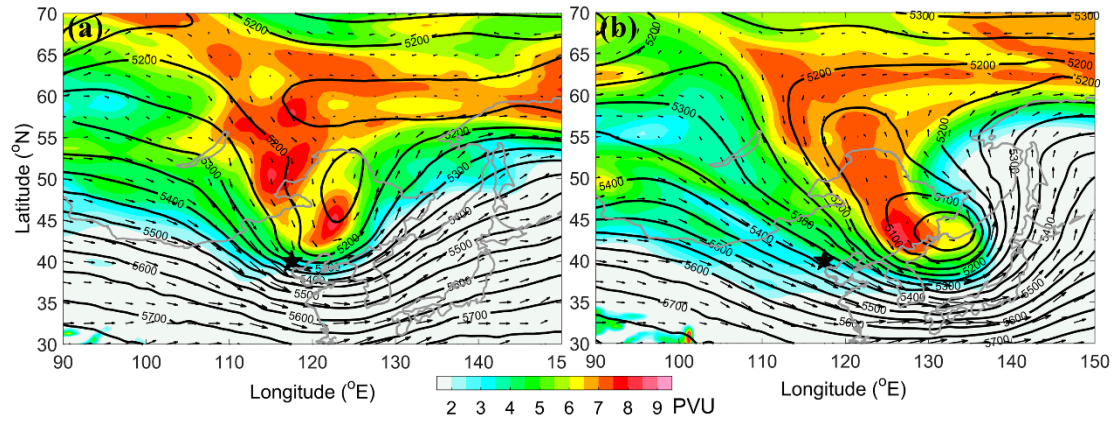
612

613 **Figures**



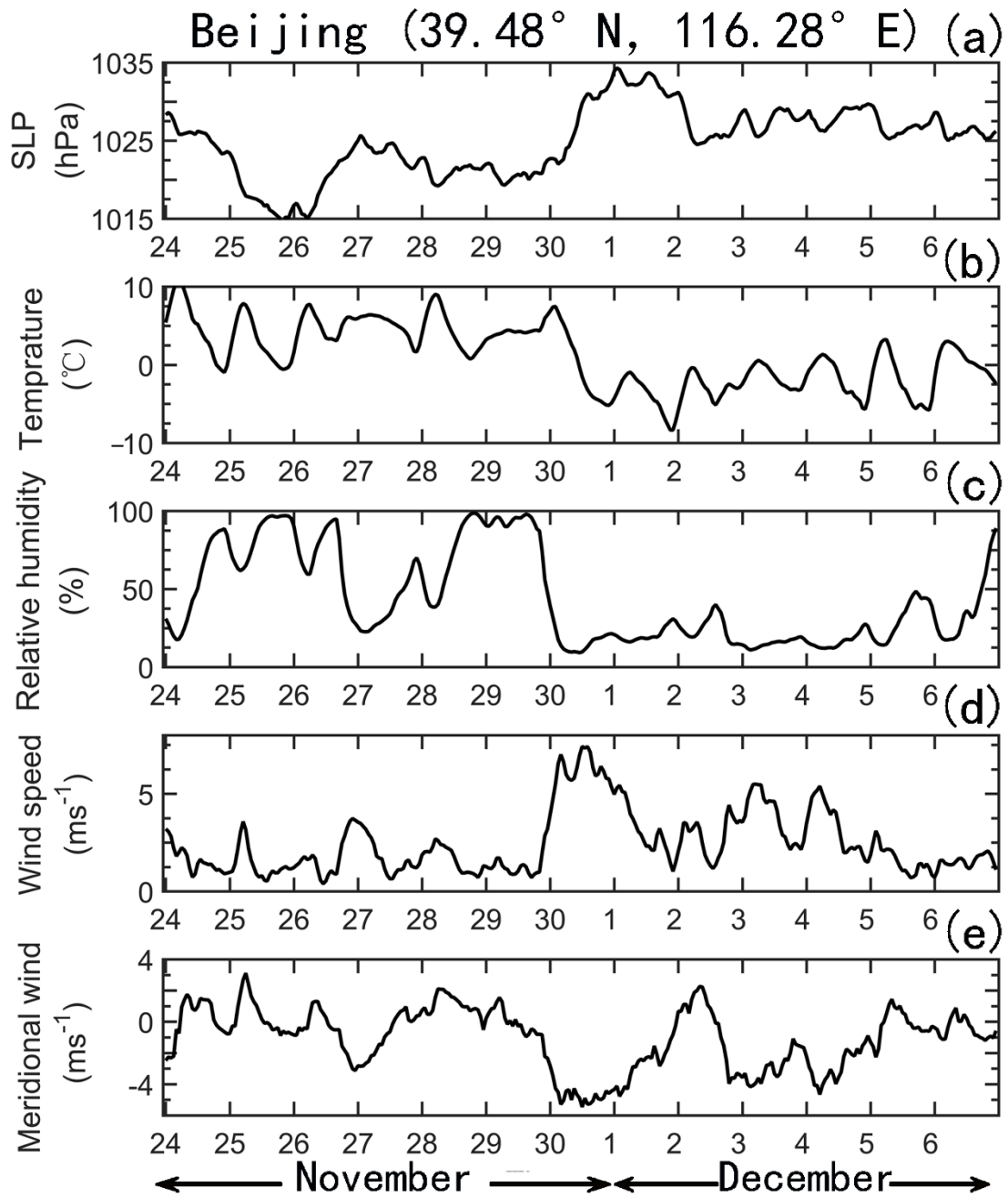
614

615 **Figure 1.** Example of the vertical height profiles of (a) the relative radar echo power
 616 (black line, smoothed by a 3-point running mean) along with its gradient variation
 617 (orange line), (b) the aspect sensitivity (black line, expressed as the ratio between the
 618 vertical echo power and oblique echo power) along with its gradient variation (orange
 619 line), observed on 12 UT 29 November 2014. The vertical profiles of simultaneous
 620 radiosonde observed temperature and potential temperature gradient are shown in plots
 621 (c) and (d). The black horizontal line denotes the LRT height derived from the
 622 radiosonde temperature profile. The orange circle indicates the RT height derived from
 623 the profile of the radar backscattered echo power.



624

625 **Figure 2.** ECMWF derived isentropic PV map on 315 K surface (shaded above 2 pvu,
 626 $1 \text{ PVU} = 10^{-6} \text{ m}^2 \text{ K kg}^{-1} \text{ s}^{-1}$) and geopotential height (contoured every 50 m in solid line)
 627 along with the wind vector (arrow) at 500 hPa ($\sim 5.5 \text{ km a.s.l.}$) on (a) 18 UTC 30
 628 November 2014, (b) 12 UTC 1 December 2014. The black star shows the location of
 629 Xianghe.



630

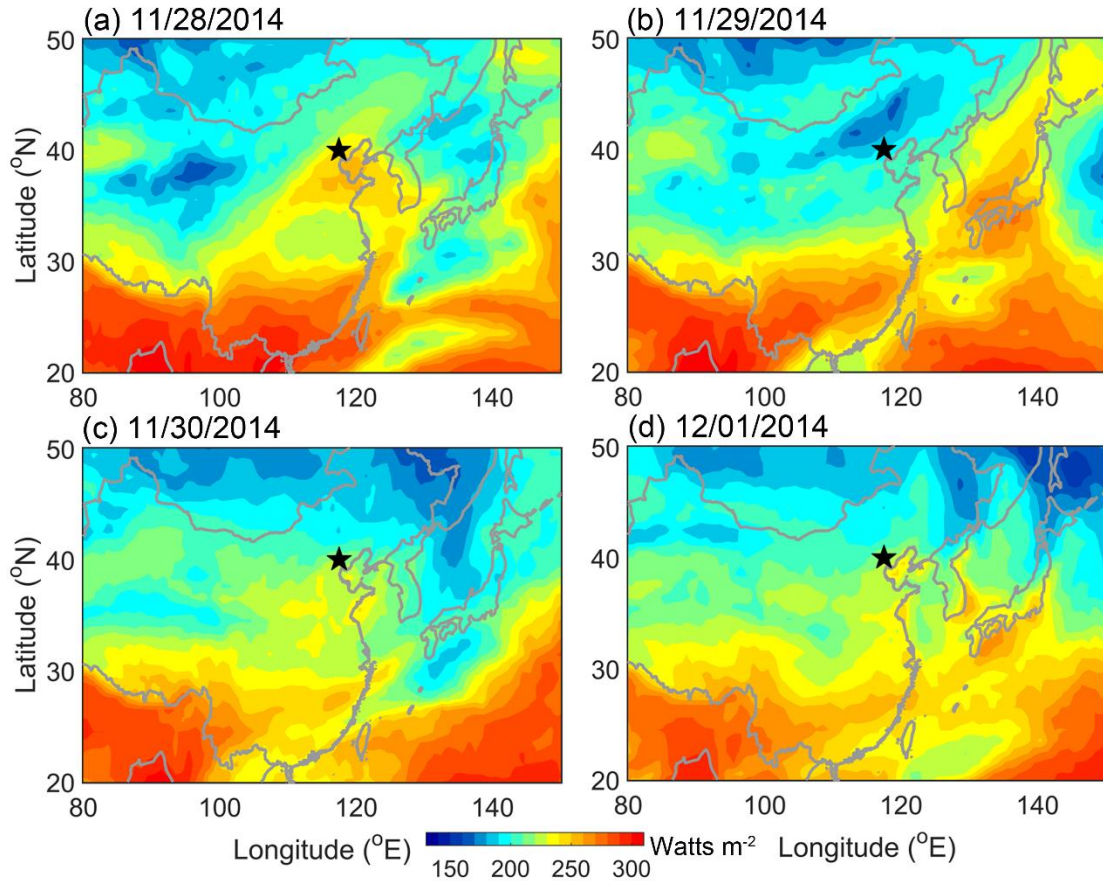
631 **Figure 3.** Time series of surface (~1.2 m above the surface) hourly meteorological

632 measurements of (a) sea level pressure, (b) temperature, (c) relative humidity, (d)

633 horizontal wind, and (e) meridional wind during the period 24 November-6 December

634 2014, observed over the Beijing station (39.4° N, 116.2° E, 31.3 m above sea level).

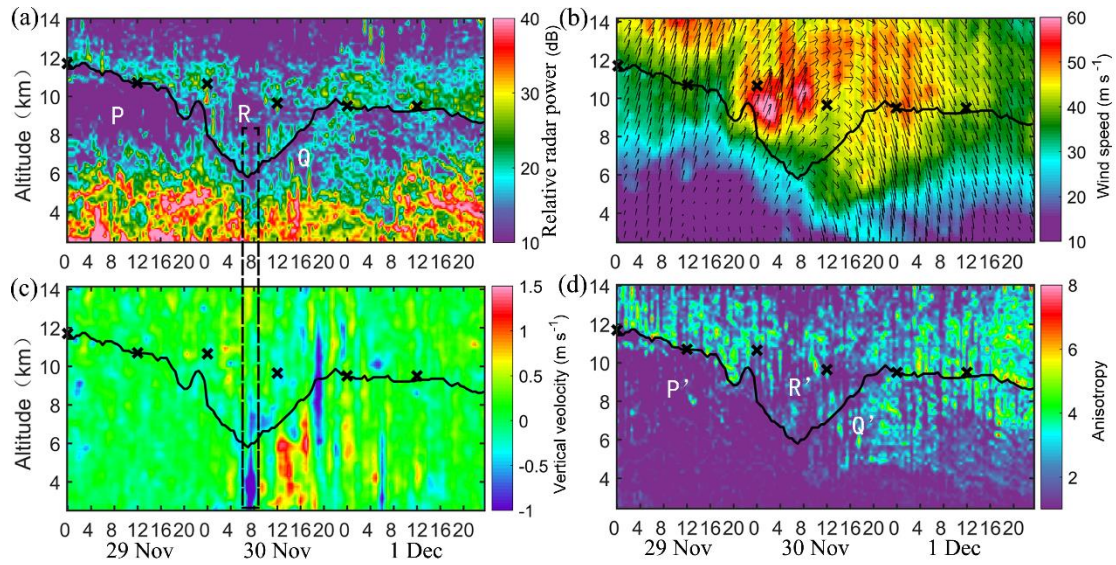
635



636

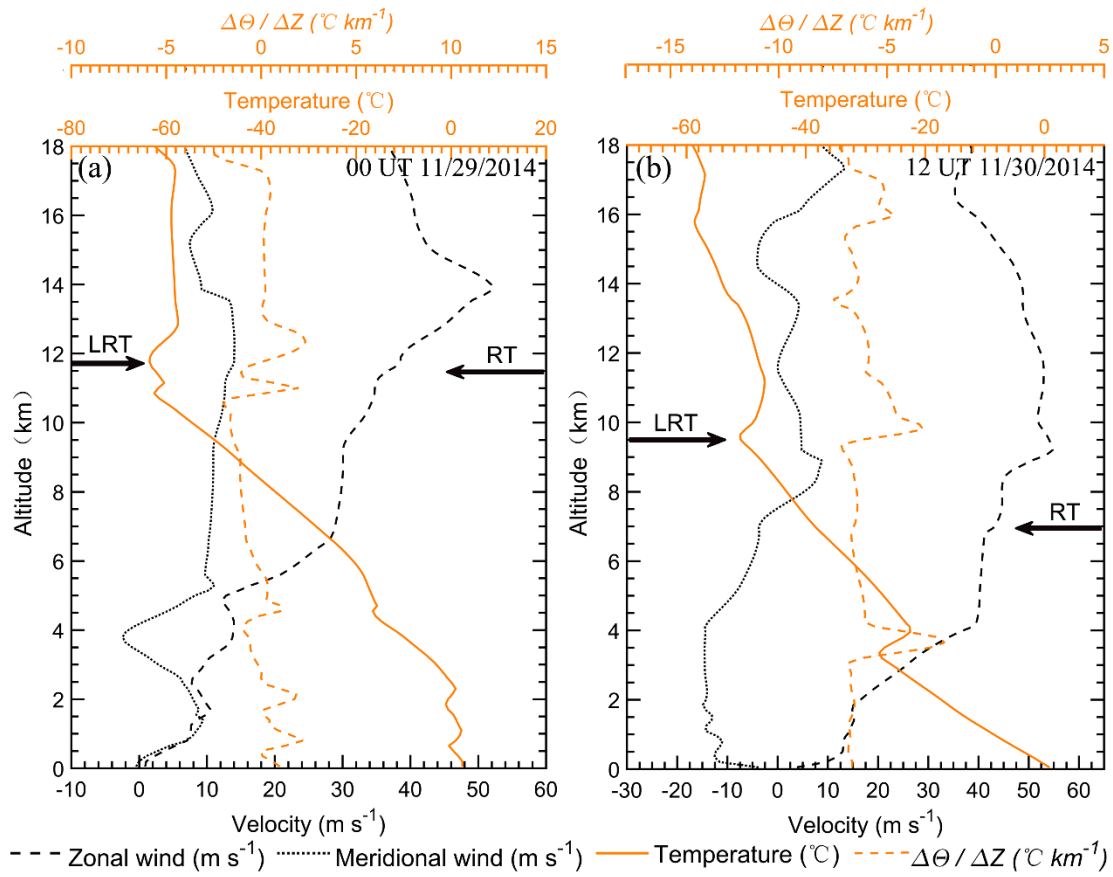
637 **Figure 4.** Contour maps of the high quality Climate Data Record (CDR) of the daily
 638 Outgoing Longwave Radiation (OLR), derived from the NOAA high-resolution
 639 infrared radiation sounder (HIRS) on (a) 28 November, (b) 29 November, (c) 30
 640 November, and (d) 1 December 2014. The black star shows the location of Xianghe.

641

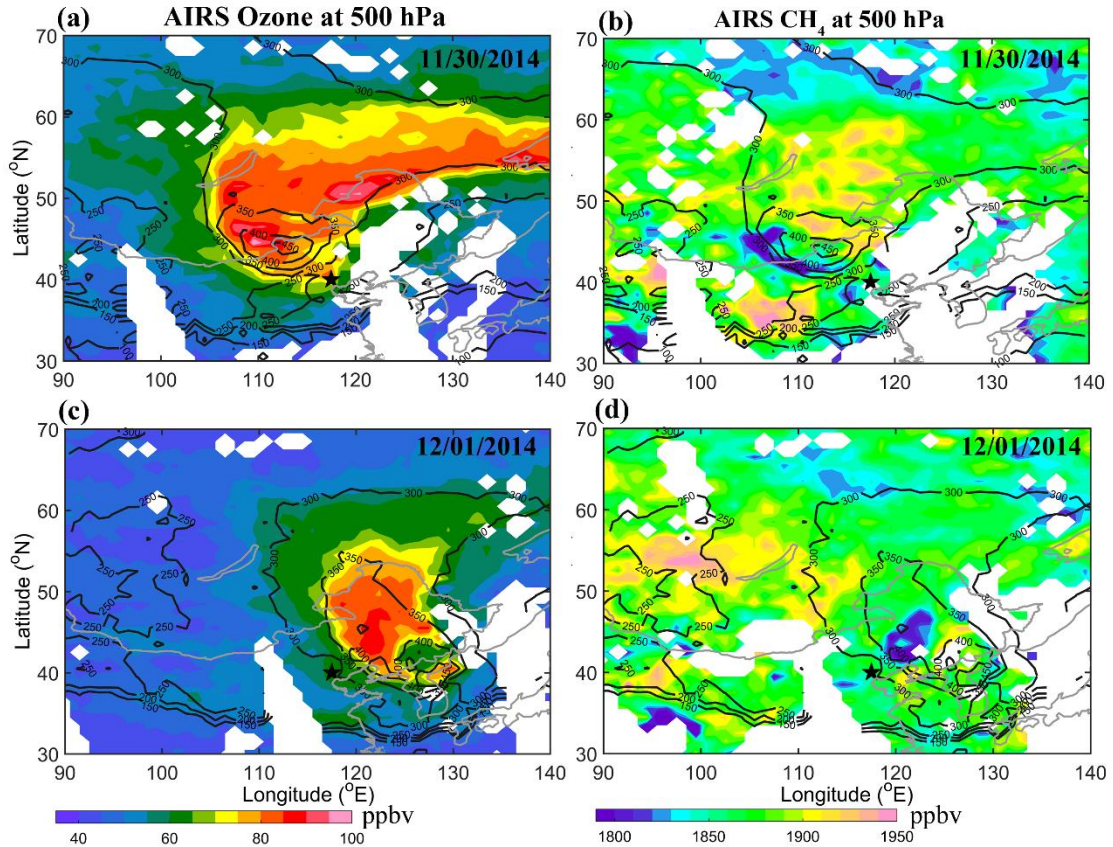


642

643 **Figure 5.** Altitude-time section of (a) the radar backscattered echo power in zenith
 644 direction, (b) the horizontal wind speed along with wind vector, of which the up and
 645 down arrows represent north and south respectively, and left-right is west-east, (c) the
 646 vertical velocity, and (d) the aspect sensitivity, observed by the Beijing MST radar from
 647 29 November to 1 December 2014. The black curve shows the radar-determined
 648 tropopause, as defined in section 2.1. The dotted rectangle highlights the strong
 649 downdrafts immediately preceding the rapid tropopause ascent. The positions of the
 650 LRT tropopause heights, derived from the nearly simultaneous collocated GPS
 651 radiosonde temperature profile, are marked by crosses.



652
 653 **Figure 6.** Vertical profiles of zonal wind, meridional wind, temperature, and potential
 654 temperature gradient derived from the GPS radiosonde measurements, at (a) 0000 UTC
 655 29 November 2014 and (b) 1200 UTC 30 November 2014. The bold arrows on the left
 656 and right side of each panel indicate the radiosonde derived LRT tropopause and radar-
 657 derived tropopause height, respectively.
 658



659

660 **Figure 7.** 500 hPa Ozone (left panels) and methane CH₄ (right panels) distribution

661 along with the tropopause height contour, derived from the AIRS satellite observations.

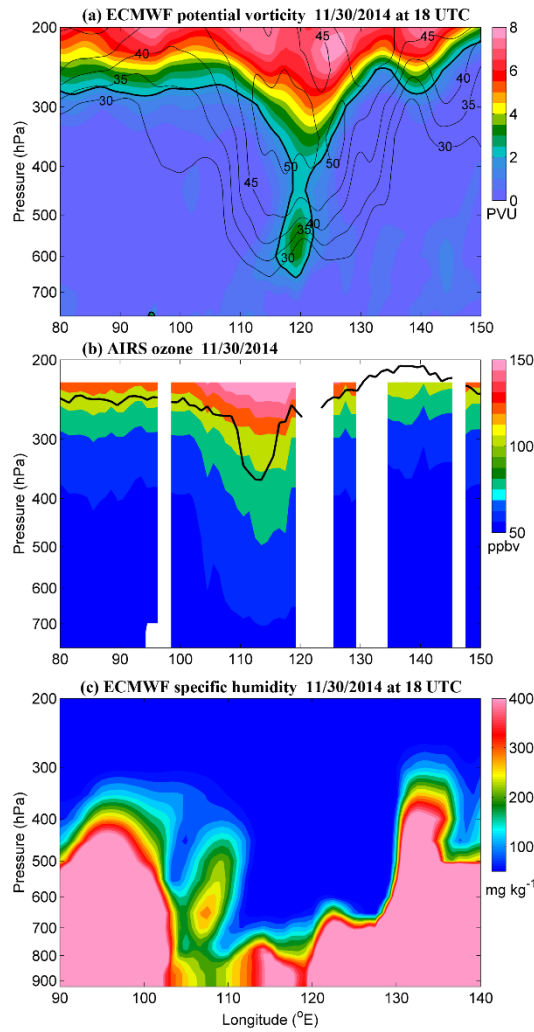
662 The top and bottom plots show the data of 30 November 2014 and 1 December 2014,

663 respectively. According to the Aqua Orbit Tracks (not shown), the time range of the

664 satellite passage is between ~04:00-07:25 on 30 November and between ~03:15-06:35

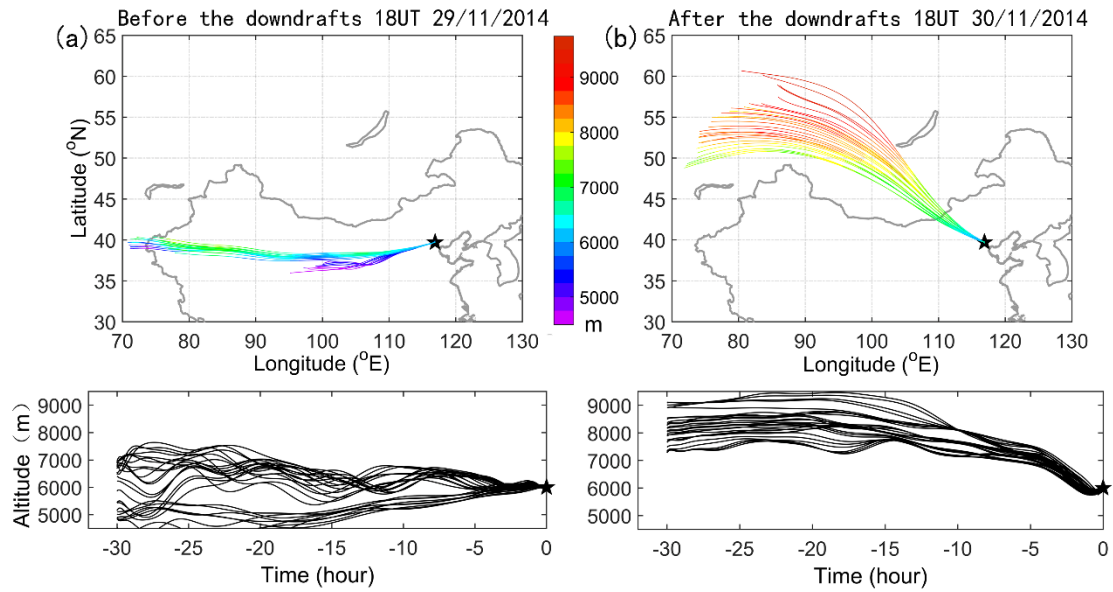
665 on 1 December 2014. The black star indicates the location of Xianghe.

666



667

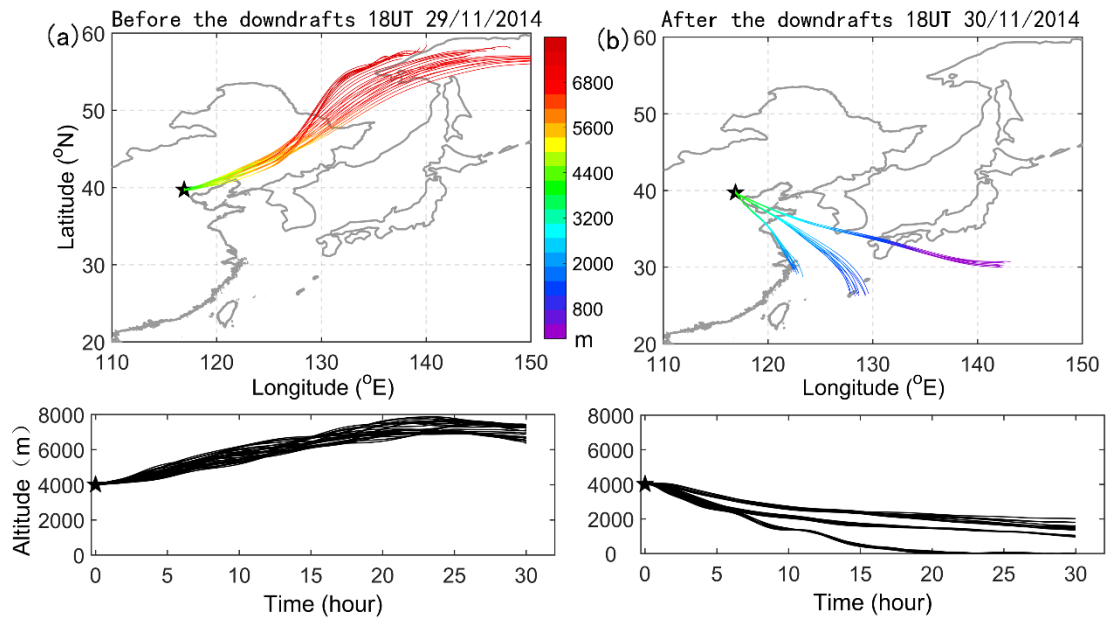
668 **Figure 8.** Longitude-pressure cross section of (a) ECMWF PV (colors, in pvu) along
 669 with horizontal wind contour (thin black line, m/s) at 18 UTC on 30 November 2014,
 670 (b) AIRS ozone mixing ratio (colors, in ppbv) along with tropopause height (black line)
 671 on 30 November 2014, and (c) ECMWF specific humidity (colors, in mg kg^{-1}) at 18
 672 UTC on 30 November 2014, at a constant latitude 40° N (nearest grid point in the
 673 latitude of Xianghe). The bold line in (a) marks the isotropic line of PV at 2 pvu.



674

675 **Figure 9.** Illustration of 30 h three-dimensional backward trajectories ending at
 676 Xianghe at 6000 m using National Oceanic Atmospheric Administration (NOAA)
 677 HYSPLIT model: (a) before the main downdrafts at 18 UTC on 29 November 2014,
 678 and (b) after the main downdrafts at 18 UTC on 30 November 2014. The HYSPLIT
 679 ensemble consists of 27 trajectories. Upper plots show the horizontal projection of the
 680 trajectories, and the lower plots show the corresponding time-height vertical
 681 displacement of the trajectories.

682

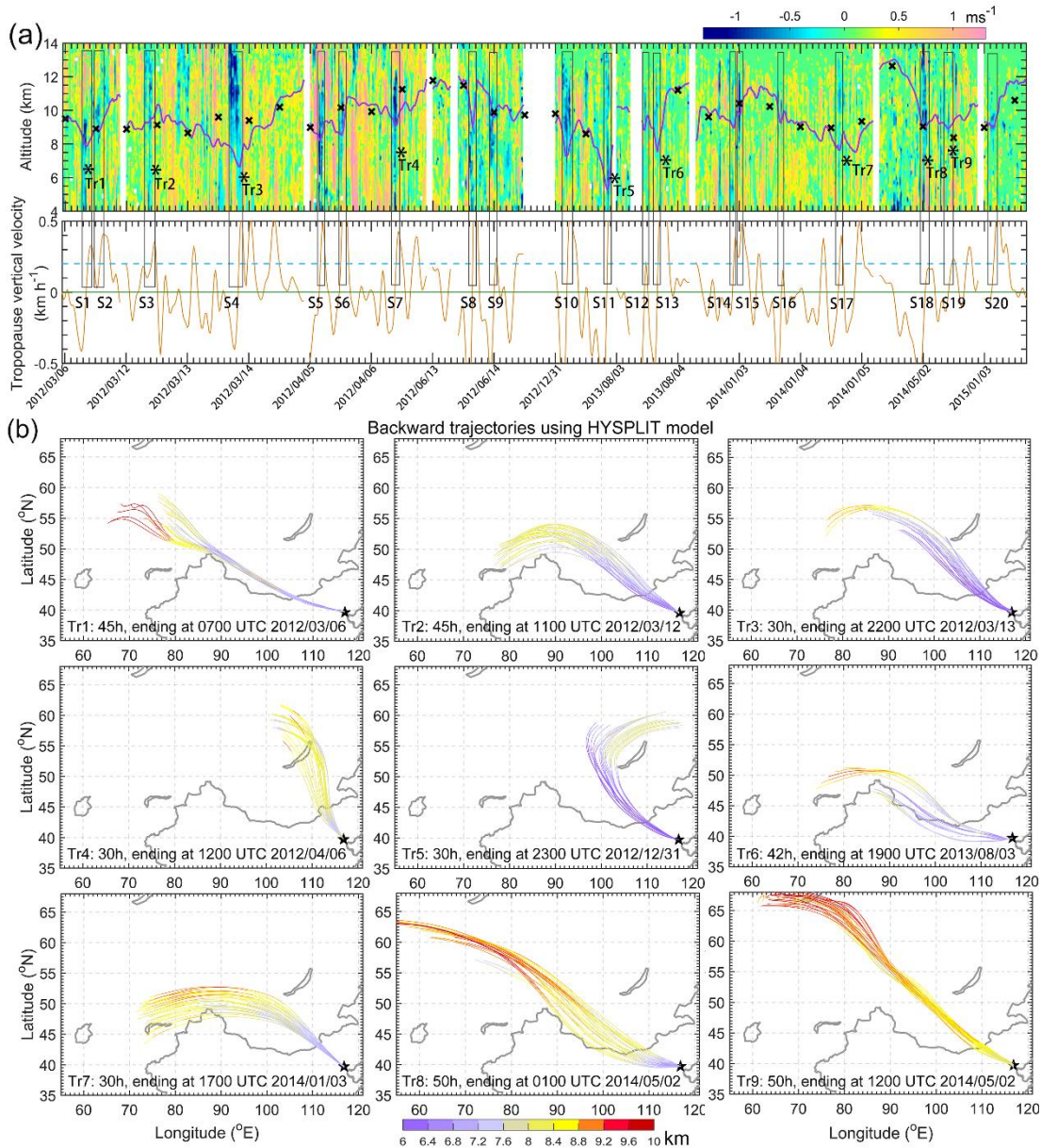


683

684 **Figure 10.** Same as Fig.10 but for three-dimensional forward trajectories starting at

685 Xianghe at 4000 m: (a) before the main downdrafts at 00 UTC on 30 November 2014,

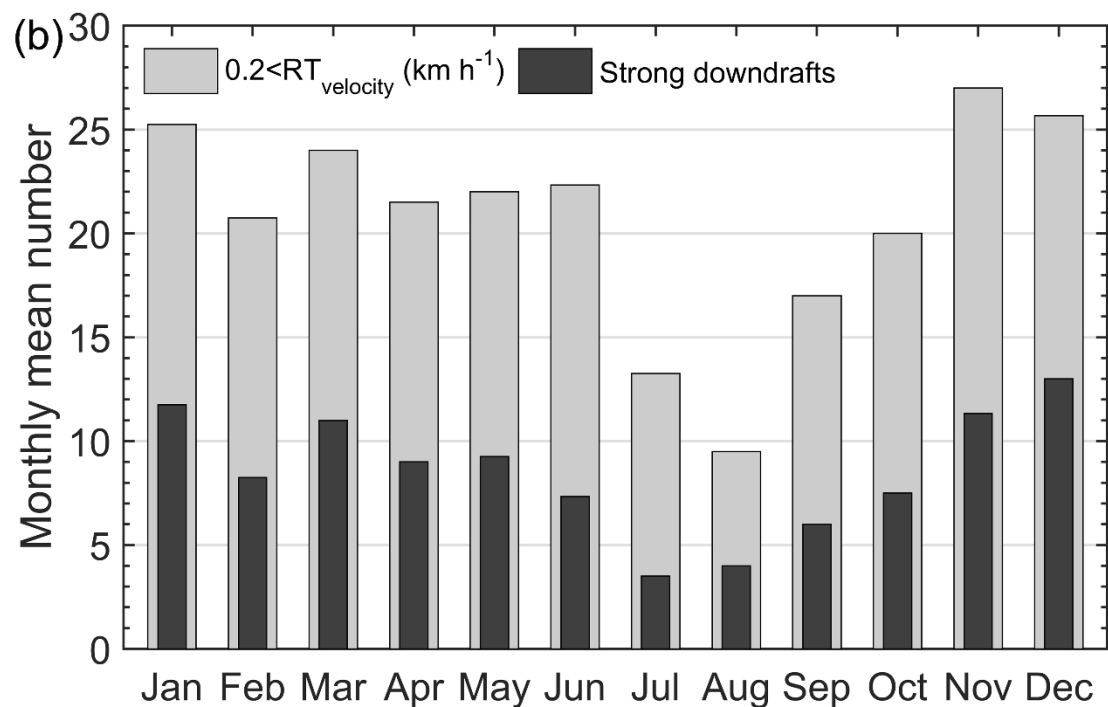
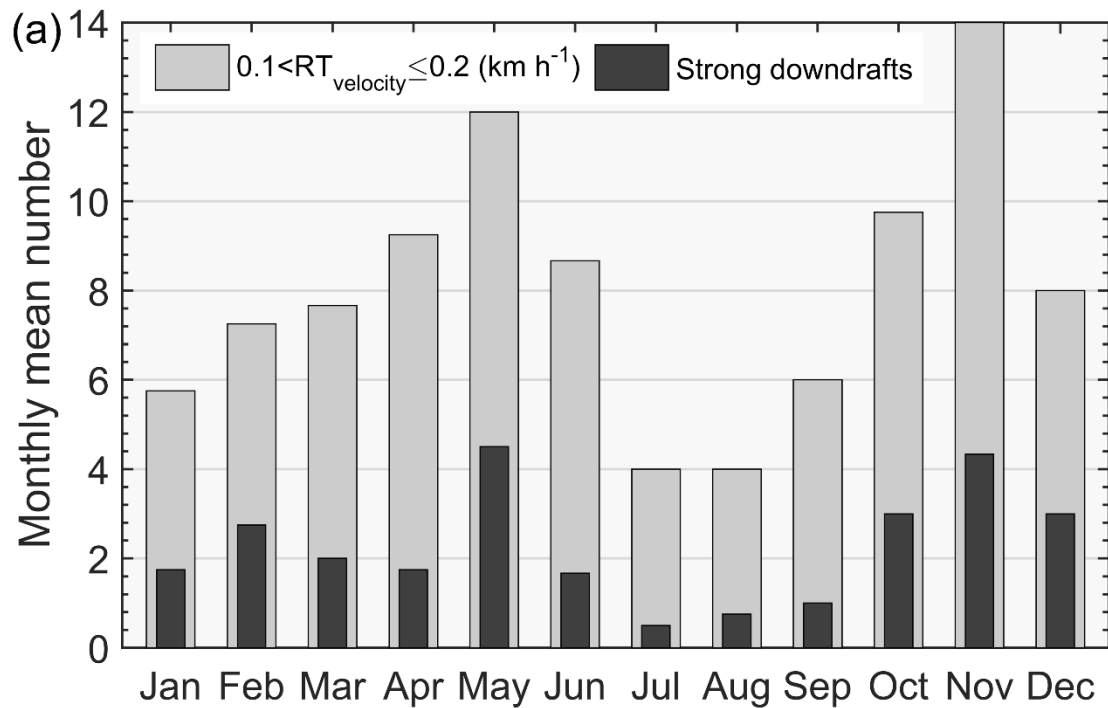
686 and (b) after the main downdrafts at 00 UTC on 1 December 2014.



687

688 **Figure 11.** (a) Height-time section of several episodic observations of the radar-derived
 689 vertical wind (colors in m/s) along with RT height (purple bold line) and LRT height
 690 (bold crosses), between March 2012 and Jan. 2015. The corresponding vertical velocity
 691 of the RT (orange line) is plotted in the lower panel of (a), dotted blue line indicates the
 692 value of 0.2 km/h. Dates for the observations are displayed as year/month/day. Black
 693 rectangular boxes represent the cases of strong downdraughts (absolute value ≥ 0.5 m/s)
 694 preceding rapid tropopause ascent (>0.1 km h⁻¹) and are labeled as S1, S2, S3..., S20.

695 Symbol ‘*’ labeled as Tr1-Tr9 indicates the ending point of the corresponding
696 trajectories in Fig.12b. (b) Results of backward trajectories (colors in km) of the typical
697 9 selecting cases from Fig.12a, providing the signature and source of possible
698 stratospheric intrusions.
699



700

701 **Figure 12.** Four years (2012-2015) of radar-determined monthly mean number of rapid

702 tropopause ascent (gray bands) and the corresponding strong downdrafts just preceding

703 the rapid tropopause ascent (black bands). (a) Gray bands: with the ascent by at least

704 0.6 km and the excursion velocity is between 0.1-0.2 km h⁻¹; black bands: except for

705 the criteria of gray bands, strong downdrafts occurred preceding the rapid RT ascent

706 must exceed 0.5 m s^{-1} and pass through the RT layer. (b) Same as (a) but for the
707 occasions when the ascent velocity is larger than 0.2 km h^{-1} . According to the study
708 here, the black bands in the histogram well represent the occurrence of possible
709 stratospheric intrusions.